# Spatial-temporal consistency between gross primary productivity and solar-induced chlorophyll fluorescence of vegetation in China during 2007–2014

Jun Ma [a], Xiangming Xiao [a,b,*], Yao Zhang [b], Russell Doughty [b], Bangqian Chen [c], Bin Zhao [a]

[a] Ministry of Education Key Laboratory for Biodiversity Science and Ecological Engineering, Shanghai Chongming Dongtan Wetland Ecosystem Research Station, Shanghai Institute of Eco-Chongming (SIEC), Fudan University, Shanghai 200433, China
[b] Department of Microbiology and Plant Biology, Center for Spatial Analysis, University of Oklahoma, Norman, OK 73019, USA
[c] Danzhou Investigation & Experiment Station of Tropical Cops, Ministry of Agriculture, Rubber Research Institute, Chinese Academy of Tropical Agricultural Sciences (CATAS), Danzhou 571737, China

## HIGHLIGHTS

- VPM-based GPP is consistent with GOME-2 SIF at multiple spatial-temporal scales
- Large spatial-temporal variations exist in terrestrial GPP of China during 2007–2014
- Satellite-based SIF data has great potential in simulating GPP at large spatial scales

## GRAPHICAL ABSTRACT
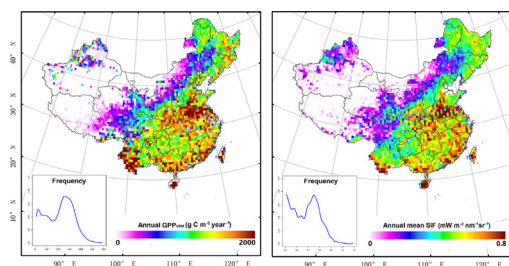


## ARTICLE INFO

## ABSTRACT

Accurately estimating spatial-temporal patterns of gross primary production (GPP) is important for the global carbon cycle. Satellite-based light use efficiency (LUE) models are regarded as an efficient tool in simulating spatial-temporal dynamics of GPP. However, the accuracy assessment of GPP simulations from LUE models at both spatial and temporal scales remains a challenge. In this study, we simulated GPP of vegetation in China during 2007–2014 using a LUE model (Vegetation Photosynthesis Model, VPM) based on MODIS (moderate-resolution imaging spectroradiometer) images with 8-day temporal and 500-m spatial resolutions and NCEP (National Center for Environmental Prediction) climate data. Global Ozone Monitoring Instrument 2 (GOME-2) solar-induced chlorophyll fluorescence (SIF) data were used to compare with VPM simulated GPP ($GPP_{VPM}$) temporally and spatially using linear correlation analysis. Significant positive linear correlations exist between monthly $GPP_{VPM}$ and SIF data over a single year (2010) and multiple years (2007–2014) in most areas of China. $GPP_{VPM}$ is also significantly positive correlated with GOME-2 SIF ($R^2 > 0.43$) spatially for seasonal scales. However, poor consistency was detected between $GPP_{VPM}$ and SIF data at yearly scale. GPP dynamic trends have high spatial-temporal variation in China during 2007–2014. Temperature, leaf area index (LAI), and precipitation are the most important factors influence $GPP_{VPM}$ in the regions of East Qinghai-Tibet Plateau, Loss Plateau, and Southwestern China, respectively. The results of this study indicate that $GPP_{VPM}$ is temporally and spatially in line with GOME-2 SIF data, and space-borne SIF data have great potential for evaluating LUE-based GPP models.

© 2018 Elsevier B.V. All rights reserved.

* Corresponding author at: Songhu Rd. 2005, Ministry of Education Key Laboratory for Biodiversity Science and Ecological Engineering, School of Life Science, Fudan University, Shanghai 200438, China.
E-mail address: Xiangming.xiao@ou.edu (X. Xiao).

## 1. Introduction

Terrestrial vegetation sequesters carbon dioxide through photosynthesis, which is measured as vegetation productivity, and is the largest $CO_2$ flux in global carbon cycle (Yang et al., 2015). It provides energy and matter for the biosphere and supports most life on Earth (Demmig-Adams and Adams, 2000). Vegetation productivity is usually measured as gross primary production (GPP), which is the total amount of carbohydrate that is assimilated by vegetation. Because of its importance in global carbon cycle, numerous studies have assessed the impacts of climate change on GPP (Ciais et al., 2005; Rogers et al., 2017; Sitch et al., 2003; Y.L. Zhang et al. 2014). In particular, increased carbon uptake by vegetation has played an important role in mitigating negative social and ecological effects caused by increased atmospheric $CO_2$ concentration and temperature in the past several decades (Ballantyne et al., 2012). Accurately estimating GPP at regional and global scales has been vital in understanding the role that terrestrial vegetation plays in the carbon cycle and how ecosystems and climate interact, especially during extreme climate events (Zhang et al., 2016c).

Many approaches have been developed to estimate GPP of terrestrial ecosystems. Satellite-based production efficiency models (PEMs) is a popular approach that is based on light-use efficiency (LUE) (Monteith, 1972; Wagle et al., 2016) to estimate GPP at various spatial and temporal scales. GPP calculated by this method is based on photosynthetically active radiation (PAR), the fraction of absorbed PAR (fPAR) by vegetation, and LUE. Generally, fPAR can be defined at either the canopy or chlorophyll scale and is often approximated by various vegetation indices from remote sensing images using two different satellite-based LUE models. One type of LUE model (e.g., MODIS-PSN model and EC-LUE model) estimates GPP by regarding fPAR as the fraction of PAR absorbed by vegetation canopy (fPAR$_{canopy}$), which is usually derived from normalized difference vegetation index (NDVI) or leaf area index (LAI) (Potter et al., 1993; Running et al., 2004; Yuan et al., 2007). The second type of LUE models (e.g., the vegetation production model, VPM) considers the fraction of PAR absorbed by vegetation chlorophyll (fPAR$_{chl}$) in the estimation of GPP, and the enhanced vegetation index (EVI) is generally used to estimate fPAR$_{chl}$ (Wu et al., 2011; Xiao et al., 2004a; Xiao et al., 2004b). For example, VPM has been used to simulate GPP for different ecosystems (such as forests, croplands, savannas, and grasslands) over many years using climate data (Dong et al., 2015; Jin et al., 2013; Kalfas et al., 2011; Wagle et al., 2014; Xiao et al., 2005), and the results were identified to be highly consistent with observed data from eddy covariance (EC) tower sites. However, considerable variance exists in the performance of LUE-based GPP models at regional and global scales in major biomes (Jung et al., 2007; Li et al., 2014; Nightingale et al., 2007), and the main reasons include their differences in model structure, model parameters, and input datasets (Hilker et al., 2008; Jin et al., 2015).

Satellite-based PEMs have a great ability to monitor GPP spatially and temporally. However, it is hard to evaluate the simulated GPP results due to the lack of observational data at relevant spatial and temporal scales (Yuan et al., 2016). In-situ GPP estimates are typically calculated using net ecosystem $CO_2$ exchange (NEE) data collected at EC tower sites by partitioning of NEE into GPP and ecosystem respiration ($R_e$) (Baldocchi et al., 2001). These GPP calculations from EC tower sites (GPP$_{EC}$) have been up-scaled by previous studies to regional scales using machine learning methods so that GPP$_{EC}$ data could be compared with PEMs simulated GPP results (Jung et al., 2009; Jung et al., 2011; Xiao et al., 2014; Xiao et al., 2010). Upscaling of GPP$_{EC}$ to regional GPP generally involves using regression algorithms, satellite-based vegetation indices (VIs), and climate data. The application of this approach is limited due to the availability of GPP$_{EC}$ data and the uncertainties of vegetation indices and climate data. At regional or global scales, several LUE-based models were used to estimate global GPP in recent studies (Chen et al., 2014; He et al., 2014; Zhang et al., 2016b;

Zhang et al., 2016c), but the validation of these models is still challenging.

Chlorophyll fluorescence in the red and near infrared bands (with wavelength of 650–800 nm) is emitted during the vegetative photochemical energy process and directly reflects the intensity of photosynthesis (Liu and Cheng, 2010). Solar-induced chlorophyll fluorescence (SIF) has recently been measured by multiple satellite-based instruments including the Greenhouse Gases Observing Satellite (GOSAT) (Frankenberg et al., 2011; Guanter et al., 2012; Joiner et al., 2011), the Global Ozone Monitoring Instrument-2 (GOME-2) (Joiner et al., 2013), and the Orbiting Carbon Observatory-2 (OCO-2) (Frankenberg et al., 2014). These space-borne SIF data have a great potential in estimating photosynthesis at regional and global scales (Frankenberg et al., 2011; Guanter et al., 2014). For example, a previous study found that SIF can be used as a proxy for GPP due to its relationship with both APAR and LUE (Yang et al., 2015). Moreover, SIF data was shown to have potential in improving carbon cycle modeling and predicting agricultural productivity (Guan et al., 2016). Both SIF and GPP are related to light absorption processes of photosynthesis (APAR or fPAR) (Wagle et al., 2016), and space-borne SIF is regarded as the direct observation of the photosynthetic process. Therefore, it is appropriate to compare space-borne SIF data with LUE-based GPP simulations for validation at regional and global scales.

Although a good consistency between seasonal LUE-based models (such as VPM) simulated GPP and SIF data was identified for a single year. However, considering climate change and land use change, which has significant impact on GPP estimate and SIF measurement, varies among years. The performance of the consistency between GPP and SIF at seasonal scale for multiple years as well as at interannual scale is still unclear. Besides, as GPP plays a central role in global carbon cycles, studies of the dynamic and trend of GPP can give useful information in estimating global carbon budget. Furthermore, to our knowledge, few studies have been conducted to evaluate the performance of LUE-based models and GPP estimates in China using space-borne SIF data. Therefore, the objectives of this study were to (1) use VPM to simulate time-series GPP of China from 2007 to 2014; (2) compare VPM simulated GPP and GOME-2 SIF data at 0.5° (latitude/longitude) resolution for China at monthly, seasonal, and annual timescales for 2007–2014; and (3) explore the interannual variability of GPP in different periods during 2007–2014 in China. Considering that SIF data directly reflects the intensity of photosynthetic activity, the data can be used to evaluate, improve, and identify possible source of errors in VPM simulations by locating those regions and biomes where the consistency between GPP and SIF is good or poor. Also, quantitative comparison of GPP between China and other regions with similar land cover types and latitude ranges can give better understand the spatial distribution of global carbon cycle.

## 2. Materials and methods

### 2.1. The vegetation photosynthesis model

The vegetation photosynthesis model (VPM) was developed by partitioning the total sunlight absorbed by vegetation into light absorbed by chlorophyll *a* and light absorbed by non-photosynthetic vegetation (Xiao et al., 2004a; Xiao et al., 2004b). The VPM calculates daily GPP as a product of light use efficiency (LUE, $\varepsilon_g$) and absorbed photosynthetically active radiation by chlorophyll (APAR$_{chl}$). The fraction of PAR absorbed by chlorophyll (fPAR$_{chl}$), which is estimated by a linear function of enhanced vegetation index (EVI) (Xiao et al., 2004a), is used to calculate APAR$_{chl}$. Eqs. (1)–(5) describe the main processes of GPP estimation in the VPM (Zhang et al., 2016c).

$$GPP = \varepsilon_g \times APAR_{chl} \tag{1}$$

$$APAR_{ch1} = fPAR_{ch1} \times PAR \tag{2}$$

$$fPAR_{ch1} = (EVI - 0.1) \times 1.25 \tag{3}$$

$$\varepsilon_g = \varepsilon_0 \times T_{schalar} \times W_{scalar} \tag{4}$$

where $\varepsilon_g$ is estimated as a function of the maximum light use efficiency ($\varepsilon_0$), air temperature $T_{scalar}$), and water condition ($W_{scalar}$). $T_{scalar}$ and $W_{scalar}$ are scalars for the effects of temperature and water on light use efficiency, respectively (Xiao et al., 2004a). $\varepsilon_0$ is a biome-specific parameter which differs between C3 and C4 plants.

$T_{scalar}$ is estimated from the fowling equation derived from a terrestrial ecosystem model (TEM) (Raich et al., 1991):

$$T_{scalar} = \frac{(T - T_{max}) \times (T - T_{min})}{(T - T_{max}) \times (T - T_{min}) - (T - T_{opt})^2} \tag{5}$$

where $T_{min}$, $T_{max}$, and $T_{opt}$ are the minimum, maximum, and optimum temperatures for vegetation photosynthesis, which are also biome-specific and can be obtained from a Look-Up Table (LUT) (Table S1).

$W_{scalar}$ is calculated from the land surface water index (LSWI) (Eq. 8) (Xiao et al., 2004a) using the following equation:

$$W_{scalar} = \frac{1 + LSWI}{1 + LSWI_{max}} \tag{6}$$

where $LSWI_{max}$ is the maximum LSWI (Xiao et al., 2002) during the growing season over several years, and it is set based on a series of procedures which was documented in detail in one of our previous studies (Zhang et al., 2016c).

## 2.2. Simulation of the vegetation photosynthesis model

VPM simulations are driven by vegetation indices (EVI and LSWI), climate data (PAR and temperature), and biome-specific physical parameters ($\varepsilon_0$, $T_{min}$, $T_{max}$, and $T_{opt}$). We used 8-day 500 m resolution MODIS products and Gaussian grid ($192 \times 96$; ~ $1.875° \times 2°$) National Center for Environment Prediction (NCEP) reanalysis-II climate data during 2007–2014 to drive the VPM. We obtained 8-day 500 m resolution $GPP_{VPM}$ results after the simulation. All the input data of VPM are detailed in the following subsections.

### 2.2.1. MODIS vegetation indices, land cover types, and land surface temperature data

The MODIS MOD09A1 surface reflectance product, with a spatial resolution of 500 m and an 8-day temporal resolution, were used to calculate EVI (Huete et al., 2002) and LSWI based on the following equations:

$$EVI = 2.5 \times \frac{\rho_{nir} - \rho_{red}}{\rho_{nir} + (6 \times \rho_{red} - 7.5 \times \rho_{blue}) + 1} \tag{7}$$

$$LSWI = \frac{\rho_{nir} - \rho_{swir}}{\rho_{nir} + \rho_{swir}} \tag{8}$$

where $\rho_{nir}$, $\rho_{red}$, $\rho_{blue}$, and $\rho_{swir}$ are the surface reflectance of near infrared, red, blue, and short-wave infrared band, respectively. A temporal gap-fill algorithm, which was detailed in our study (Zhang et al., 2016c), is applied to EVI time series data.

The temperature parameters in VPM are biome-specific, and we extract this information by using the IGBP land cover classification scheme in the MODIS MCD12Q1 land cover product (Friedl et al., 2010). LUT (Table S1) is used to get parameters of $\varepsilon_0$, $T_{min}$, $T_{max}$, and $T_{opt}$ for individual biomes.

The water parameter in VPM is land-surface-specific. In order to avoid the effects of snow cover in identifying yearly maximum LSWI, thermal growing season and snow cover period are differentiated based on information from the MODIS MYD11A2 land surface temperature (LST) dataset. This dataset provides surface temperature at 1:30 am local time which can be regarded as the daily minimum temperature.

The thermal growing season begins when LST of three consecutive 8-day values in the spring is above 5 °C, while the thermal growing season ends when LST of three consecutive 8-day in the fall is below 10 °C (Zhang et al., 2017).

### 2.2.2. Climate data

We used climate data (downward shortwave radiation and air temperature) from NCEP reanalysis II product, which were provided in a Gaussian grid ($192 \times 96$; ~ $1.875° \times 2°$). The original daily data were aggregated into 8-day averages to match the temporal resolution of MODIS NDVI and LSWI indices. The day-time mean air temperature was calculated by averaging temperature between 6 am to 6 pm local time. Following previous studies that reported the positive bias of the surface shortwave radiation from the NCEP data product when compared to in-situ radiation observations (Jin et al., 2015; Zhao et al., 2006), the NCEP radiation data were multiplied by 0.8 in this study (Zhang et al., 2016c).

NCEP climate data were interpolated into 500 m resolution using a nonlinear algorithm to match the MODIS data (Zhao et al., 2005). The output value of a particular pixel ($V$) is calculated as the inverse distance weighted average values of the nearest four grid cells:

$$D_i = \cos^4 \left[ \frac{\pi}{2} \times \left( \frac{d_i}{d_{max}} \right) \right] \quad i = 1, 2, 3, 4 \tag{9}$$

$$W_i = \frac{D_i}{\sum_{i=1}^{4} D_i} \tag{10}$$

$$V = \sum_{i=1}^{4} D_i \tag{11}$$

where $d_i$ is the distance between the center of the pixel and each of the four vertex grid cells from NCEP data; $d_{max}$ is the maximum distance between the four vertex NCEP grid cells; and $V_i$ is the value for the four surrounding grid cell values of NCEP data.

### 2.3. GOME-2 SIF data

The monthly GOME-2 SIF data from January 2007 to December 2014 used in this study, obtained from an instrument onboard Eumetsat's MetOp-A satellite, was publicly available at http://acdb-ext.gsfc.nasa.gov/People/Joiner/my_gifs/GOME_F/GOME-F.htm (Joiner et al., 2014). Earth radiation at the top of atmosphere in the 715–758 nm spectrum is captured by GOME-2, and radiation with wavelength around 740 nm at the far-red peak of the SIF emission is used to retrieve SIF using a principal component analysis approach to include atmospheric absorption. The final SIF data are quality-controlled to exclude the effects of heavy clouds and aggregated to monthly average values at the spatial resolution of 0.5°. Details about the SIF calculation in GOME-2 and the effects of cloud on fluorescence measurements can be found in a study (Joiner et al., 2013).

### 2.4. Comparison between $GPP_{VPM}$ and SIF data

The 8-day VPM simulated GPP ($GPP_{VPM}$) data was aggregated into monthly mean and yearly sum $GPP_{VPM}$, and maximum daily $GPP_{VPM}$ in a year was also calculated. The 500 m resolution $GPP_{VPM}$ data were reprojected and aggregated into 0.5° to match the spatial resolution of SIF data after all data processing. Yearly mean SIF and maximum daily SIF were calculated based on monthly mean SIF data. The mean values of $GPP_{VPM}$ and SIF for different seasons (spring, summer, fall, and winter) in 2010 were also calculated. The four seasons are MAM (March, April, and May of 2010), JJA (June, July, and August of 2010), SON (September, October, and November of 2010), and DJF (December of 2010, and January and February of 2011).

Comparisons between GPP$_{VPM}$ and SIF data were conducted at both single and multiple years. Considering SIF data has been proved to be linear correlated with PAR which is the direct control of GPP in VPM, linear correlation was adopted to test the relationship between VPM simulated GPP and SIF. For the single year 2010, comparisons between annual GPP$_{VPM}$ with annual mean SIF, maximum daily GPP$_{VPM}$ with maximum daily SIF, and seasonal mean GPP$_{VPM}$ with seasonal mean SIF were conducted. Pixel-wise linear correlations between monthly mean GPP$_{VPM}$ with monthly mean SIF were also calculated in 2010. For the multiple years during 2007–2014, comparisons between monthly mean GPP$_{VPM}$ with monthly mean SIF and yearly GPP$_{VPM}$ with yearly mean SIF were conducted. Similarly, pixel-wise linear correlations between GPP$_{VPM}$ and SIF at both monthly and yearly during 2007–2014 were also conducted. The distribution maps of statistical parameters such as slope and intercept regression line, $R^2$, and $P$ value of pixel-wise linear correlations were generated.

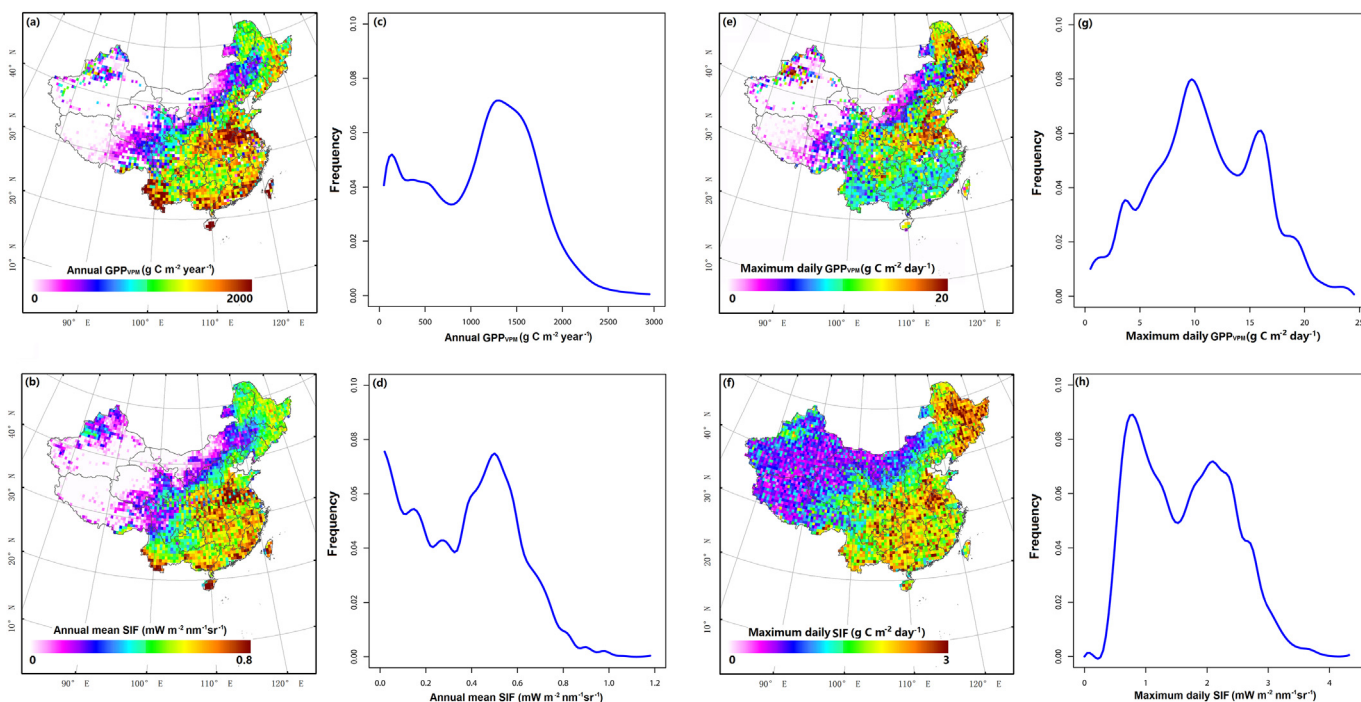## 2.5. GPP$_{VPM}$ dynamic trends and drive factors detection

The interannual trends of GPP$_{VPM}$ and SIF for China during 2007–2014 were explored in this study. Considering that climate change and land cover change occurred in China nationwide in the period of 2007–2014 (especially around the year 2010) and that GPP$_{VPM}$ had a decreasing trend during 2007–2010 and an increasing trend during 2010–2014, we assumed that climate and land cover change had significant impacts on GPP$_{VPM}$ and changed the GPP$_{VPM}$ trend around the year 2010. Therefore, linear correlations were calculated between annual GPP$_{VPM}$ and the periods of 2007–2010, 2010–2014 and 2007–2014, respectively. Pixel-wise linear correlation between annual GPP$_{VPM}$ and time for the three time periods were conducted, and the distribution maps of the slope and p-value of the regression lines were generated. In order to test and compare with other regions, annual total carbon (GPP$_{VPM}$), obtained by multiplying annual mean GPP$_{VPM}$ and the area of terrestrial land of China, was calculated for the entire study period 2007–2014. The change map of GPP$_{VPM}$ trends (pixel-wise slope map) between the periods of 2010–2014 and 2007–2010 was generated to find the spatial distribution of the change of GPP trend. Four types of GPP$_{VPM}$ trend change including continuous negative (NN), positive changed into negative (PN), negative changed into positive (NP), and continuous positive (PP) were obtained, and different types were also separated spatially in this study.

To better understand why the trend in GPP$_{VPM}$ changed in 2010, we need to identify the factors, such as climate and land cover, affected GPP$_{VPM}$. In this study, a typical point of each GPP$_{VPM}$ trend change type, except the NN type (the land surface of this type mostly is not vegetation), was selected as representative experiment site to study the relative influence of climate and land cover factors on GPP$_{VPM}$ (Fig. 8d). The typical study sites were only selected when their positions satisfy both of the following criteria: (1) located in the pixels with significant GPP$_{VPM}$ trends in both periods of 2007–2010 and 2010–2014; (2) located nearby a meteorological station (the distance is less than 10 km) so that observed climate data can be directly used.

Observed climate data (including mean daily temperature, daily precipitation, and daily illumination time) of the meteorological stations as well as remote sensing-based leaf area index (LAI) data, fraction of photosynthetically active radiation (FPAR) data (Zhu et al., 2013), with a spatial resolution of 0.083°, and the standardized precipitation-evapotranspiration index (SPEI) data (Vicente-Serrano et al., 2010) with a spatial resolution of 0.5°, from 2007 to 2014 was obtained and used as the individual variables in influencing GPP$_{VPM}$. LAI data estimates the vegetation coverage and can be used as a factor reflecting land cover change (vegetation gain or loss). FPAR and SPEI estimate the condition of solar radiation and drought, respectively, and they were direct estimation of climate condition influencing the vegetation photosynthesis process.

The observed climate data was downloaded from climate data sharing website (http://data.cma.cn/), LAI and FPAR data was obtained by contacting data producer (http://cliveg.bu.edu/modismisr/lai3g-fpar3g.html), and SPEI dataset was directly downloaded from the website (http://spei.csic.es/database.html). The daily climate data was



**Fig. 1.** The spatial distribution and frequency of average annual and maximum daily values of VPM simulated gross primary production (GPP$_{VPM}$) and sun-induced chlorophyll fluorescence (SIF) for China in 2010. (a) Spatial distribution of annual GPP$_{VPM}$; (b) spatial distribution of annual mean SIF; (c) frequency of annual GPP$_{VPM}$; (d) frequency of annual mean SIF; (e) spatial distribution of maximum daily GPP$_{VPM}$; (f) spatial distribution of maximum daily SIF; (g) frequency of maximum daily GPP$_{VPM}$; and (h) frequency of maximum daily SIF.

aggregated into monthly scale, while all raster-based data (LAI, FPAR, and $SPEI$) reprojected and aggregated into monthly 0.5° spatial-temporal scale to match the $GPP_{VPM}$ and SIF data. $GPP_{VPM}$, LAI, FPAR, and $SPEI$ data of the three study sites were obtained by extracting values of raster of the sites' position, while observed climate data of the three study sites was get directly use the recorded values of the nearby meteorological stations.

### 2.6. Statistical analysis

Boosted regression tree (BRT) analysis of generalized boosted models (GBMs) was adopted to identify the relative importance of individual climate and land cover factors on $GPP_{VPM}$. BRT analysis is a machine learning approach applied in nonlinear relationship analysis (Elith et al., 2008; Ma et al., 2017). Regression trees are originated from the theories of classification and decision tree. Boosting is mainly based on a forward procedure which constructs and combines a collection of models with the purpose of improving model performance. No transformation is needed in BRT analysis due to the ability in accommodating any data distribution. Parameters including "gaussian" error distribution, a learning rate of 0.005, a bag fraction of 0.5, and 10-fold cross validation were set in BRT analysis. Test of collinearity of all individual variables was conducted to avoid overfitting between $GPP_{VPM}$ and explanation factors. For each study site, BRT analysis was conducted, and a horizontal bar displaying the relative influence of individual variables on $GPP_{VPM}$ was obtained.

All the raster layer data processing, mapping, and statistical analysis were conducted using ArcGIS10.3 and R software (R Development Core Team, 2013), and the significance level of linear correlation is set to 0.05.

## 3. Results

### 3.1. Spatial distribution and relationship between $GPP_{VPM}$ and SIF in 2010

At the annual scale, the spatial distribution of $GPP_{VPM}$ was similar to annual mean SIF of China in 2010. The high values of annual $GPP_{VPM}$ (>2000 g C m$^{-2}$ year$^{-1}$) (Fig. 1a) and annual mean SIF (>0.8 mW m$^{-2}$ nm$^{-2}$ sr$^{-1}$) (Fig. 1b) were both distributed in South China and the North China Plains. Annual $GPP_{VPM}$ in 2010 ranged from about 100 to 1300 g C m$^{-2}$ year$^{-1}$ (Fig. 1c), while annual mean SIF in 2010 ranged from about 0.05 to 0.5 mW m$^{-2}$ nm$^{-2}$ sr$^{-1}$ (Fig. 1d). Also, maximum daily $GPP_{VPM}$ (Fig. 1e) and maximum daily SIF (Fig. 1f) in 2010 for China had similar spatial patterns for most China except for South China. Northeastern China and the North China Plain each had high

values of maximum daily $GPP_{VPM}$ (>20 g C m$^{-2}$ day$^{-1}$) and maximum daily SIF (>3 mW m$^{-2}$ nm$^{-2}$ sr$^{-1}$), while South China only had high values of maximum daily SIF. Maximum daily $GPP_{VPM}$ in 2010 ranged from about 10 to 16 g C m$^{-2}$ day$^{-1}$ (Fig. 1g), while maximum daily SIF in 2010 ranged from about 0.8 to 2.2 mW m$^{-2}$ nm$^{-2}$ sr$^{-1}$ (Fig. 1h). Significant linear correlations were found between annual $GPP_{VPM}$ and annual mean SIF ($P < 0.001$, $R^2 = 0.623$) as well as maximum daily $GPP_{VPM}$ and maximum daily SIF ($P < 0.001$, $R^2 = 0.467$) in 2010 for China (Fig. 2).

At the seasonal scale, similar spatial patterns were found between $GPP_{VPM}$ and SIF for different seasons (MAM, JJA, SON, and DJF) in 2010 for most China except for some part of South China, and significant ($P < 0.05$) linear correlations between $GPP_{VPM}$ and SIF were also identified for the four seasons. The values of the coefficient of determination for MAM, JJA, SON, and DJF were 0.60, 0.52, 0.64, and 0.37, respectively (Fig. 3).

At the monthly scale, significant ($P < 0.05$) linear correlations between monthly $GPP_{VPM}$ and monthly mean SIF were identified for all of China except for small regions in Northwestern, Southwestern, and Southern China (Fig. 4). The high correlation ($R^2 > 0.8$) was mainly distributed in Northeastern China and Central China, while the low correlation was mainly distributed in some parts of Northwest and South China.

### 3.2. Spatial-temporal relationship between $GPP_{VPM}$ and SIF during 2007–2014

At the monthly scale, significant linear correlation was found between monthly $GPP_{VPM}$ and monthly mean SIF ($P < 0.001$, $R^2 = 0.99$) during 2007–2014 using the averaged values over entire China (Fig. 5a). Except for small regions in Northwestern China, the significant ($P < 0.05$) linear correlation between monthly $GPP_{VPM}$ and monthly mean SIF during 2007–2014 was found for almost all gridcells in China (Fig. 6g). The high values of correlation efficient ($R^2 > 0.8$) was mainly distributed in Northeastern China and the Northern China Plains (Fig. 6e).

At the annual scale, significant linear correlation was found between annual $GPP_{VPM}$ and annual mean SIF ($P < 0.05$, $R^2 = 0.63$) during 2007–2014 using the averaged values across entire China (Fig. 5b). However, the significant ($P < 0.05$) linear correlation between annual $GPP_{VPM}$ and annual mean SIF during 2007–2014 can be only found for some pixels in China (Fig. 6h). The correlation ($R^2$) of all pixels in China was at very low level (Fig. 6f).
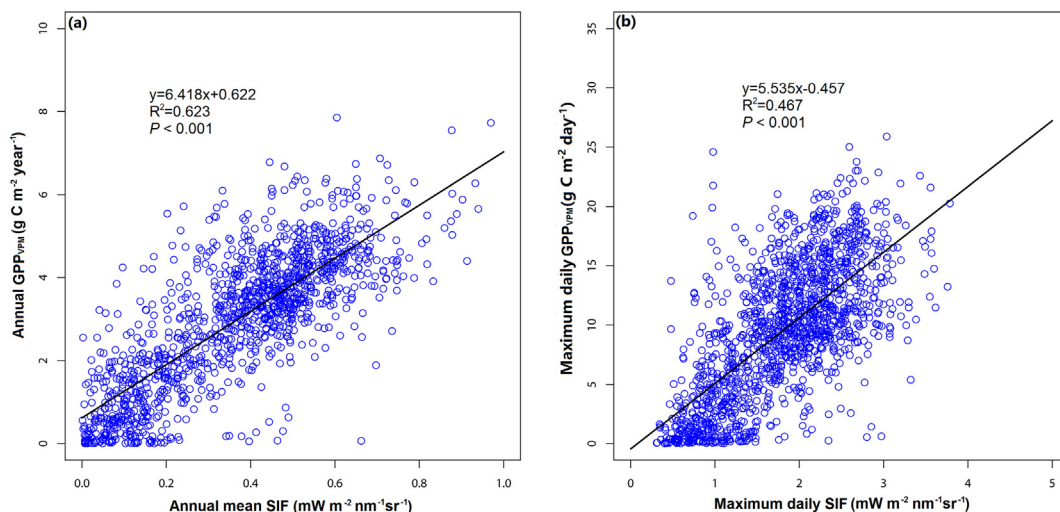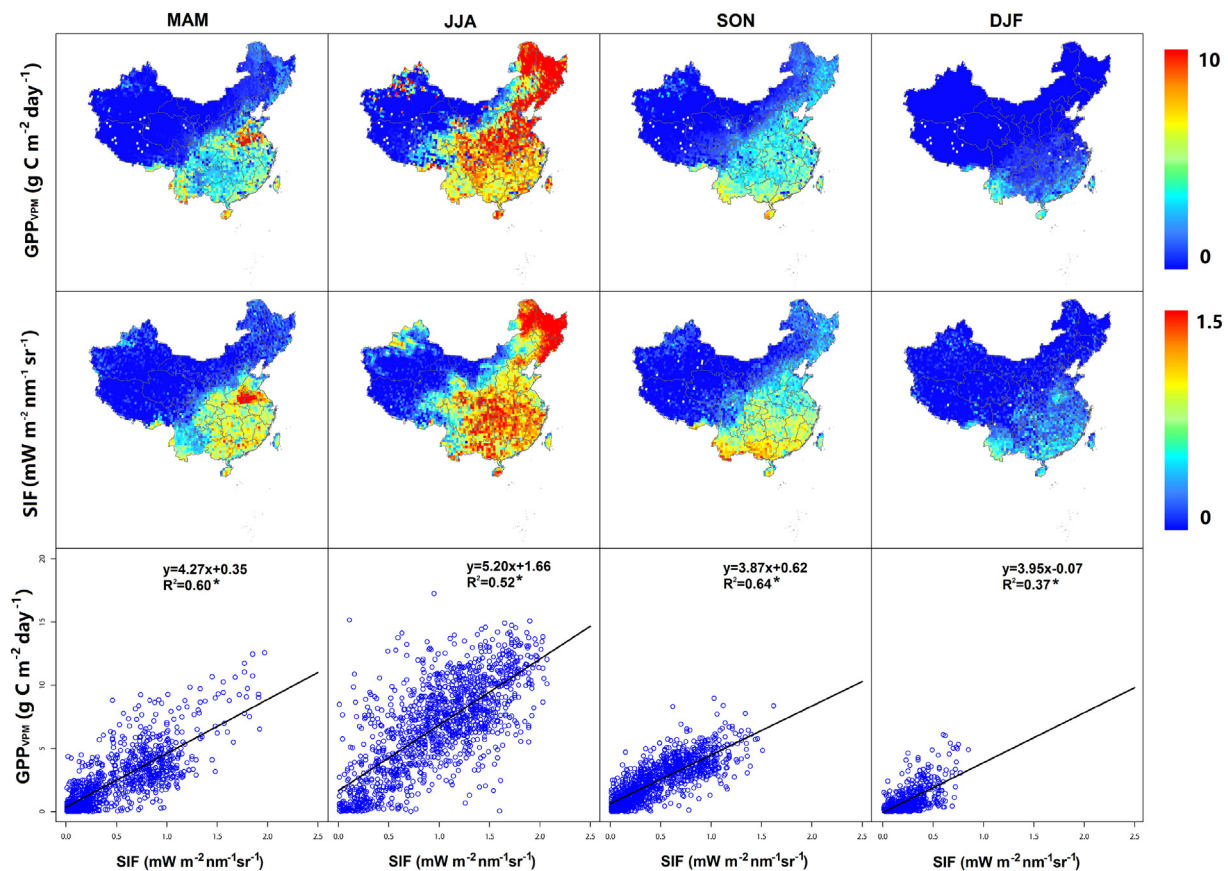


Fig. 2. Linear correlations between (a) annual $GPP_{VPM}$ (g C m$^{-2}$ year$^{-1}$) and annual mean SIF (mW m$^{-2}$nm$^{-1}$sr$^{-1}$), and (b) maximum daily $GPP_{VPM}$ (g C m$^{-2}$ day$^{-1}$) and maximum daily SIF (mW m$^{-2}$nm$^{-1}$sr$^{-1}$) in 2010 for China.

**Fig. 3.** The spatial distribution and relationships of seasonal VPM simulated gross primary production ($GPP_{VPM}$) and sun-induced chlorophyll fluorescence (SIF) for China between March 2010 and February 2011. MAM: March, April, and May; JJA: June, July, and August; SON: September, October, and November; DJF: December 2010, January, and February. R square values with a star means the linear correlation was statistically significant ($P < 0.05$).

### 3.3. Interannual $GPP_{VPM}$ dynamic and its drives during 2007–2014

For the averaged values over entire China, annual $GPP_{VPM}$ of China had a non-significant increasing trend ($P > 0.05$, $R^2 = 0.24$) over the entire study period 2007–2014. However, a significant decreasing trend ($P < 0.05$, $R^2 = 0.63$) in $GPP_{VPM}$ was found during 2007–2010, and a significant increasing trend ($P < 0.05$, $R^2 = 0.65$) was found during 2007–2010 and 2010–2014 (Fig. 7a). Besides, annual mean SIF showed a similar interannual dynamic trend as annual $GPP_{VPM}$ (Fig. 7a). Total sequestrated carbon, calculated as the sum of GPP, for China had the same trend as annual mean $GPP_{VPM}$ during 2007–2014 with the lowest value of 7.24 Pg C in 2010 and the highest value of 7.90 Pg C in 2013 (Fig. 7b).

Geographically, in the period of 2007–2014, positive $GPP_{VPM}$ trend was mainly distributed in Northern China, while negative GPP trend was mainly found in Southern and Southwestern China (Fig. 8a). Negative $GPP_{VPM}$ trend was found in most areas of China except for an increasing trend was found in Eastern Qinghai-Tibet Plateau in the period of 2007–2010 (Fig. 8c). Conversely, positive GPP trend was identified in almost all regions of China except for a decreasing trend was identified in Eastern Qinghai-Tibet Plateau in the period of 2010–2014 (Fig. 8e). Areas with significant $GPP_{VPM}$ trend in the periods of 2007–2014, 2007–2010, and 2010–2014 were mainly located some parts of Loss Plateau, in Eastern Qinghai-Tibet Plateau and Southwest China, and in some regions of North China, respectively (Fig. 8b, d, e).

The spatial distribution of different $GPP_{VPM}$ trend change types for 2007–2010 and 2010–2014 and relevant selected typical study sites was shown in Fig. 9a. NN, PN, NP, and PP types were mainly found in Northwest China, in Eastern Qinghai-Tibet Plateau, in some areas of Loss plateau of China, and in North China, respectively. Especially, PN and PP types presented highly concentrated distribution in space. Mean monthly temperature, LAI, and monthly total precipitation were the most important factors influence $GPP_{VPM}$ of the typical study sites in $GPP_{VPM}$ trend change types of PN, PP, and NP. There relative influence was 43.75%, 35.96%, and 41.21%, respectively (Fig. 9b-d). The total relative influence of the top five most important factors influence $GPP_{VPM}$ dynamics of $GPP_{VPM}$ trend change type of PN, PP, and NP were 95.49%, 97.85%, and 92.78%, respectively.

## 4. Discussion

### 4.1. Spatial-temporal consistency between $GPP_{VPM}$ and GOME-2 SIF data

Spatial distributions and frequency distributions of annual $GPP_{VPM}$ and annual mean SIF in 2010 are quite similar (Fig. 1), and the annual $GPP_{VPM}$ is significantly positively linearly correlated with annual mean SIF in 2010 ($R^2 = 0.62$, $P < 0.001$). This correlation demonstrates that the VPM simulated GPP is consistent with GOME-2 SIF data at annual scale in China, which was also shown to be true for North America (Zhang et al., 2016c). Moreover, a significant positive linear correlation exists between maximum daily $GPP_{VPM}$ and SIF in 2010 ($R^2 = 0.47$, $P < 0.001$) for China. Some areas, especially in Southern China (Fig. 1), had high maximum daily SIF values that were not reflected in the map of maximum daily $GPP_{VPM}$. This difference suggests that the performance of VPM in modeling maximum carbon uptake intensity at some low latitude areas is weak, which has been reported in previous VPM simulations at the site level (Wu et al., 2010; Yan et al., 2009). The most likely reason for this weak performance is that maximum
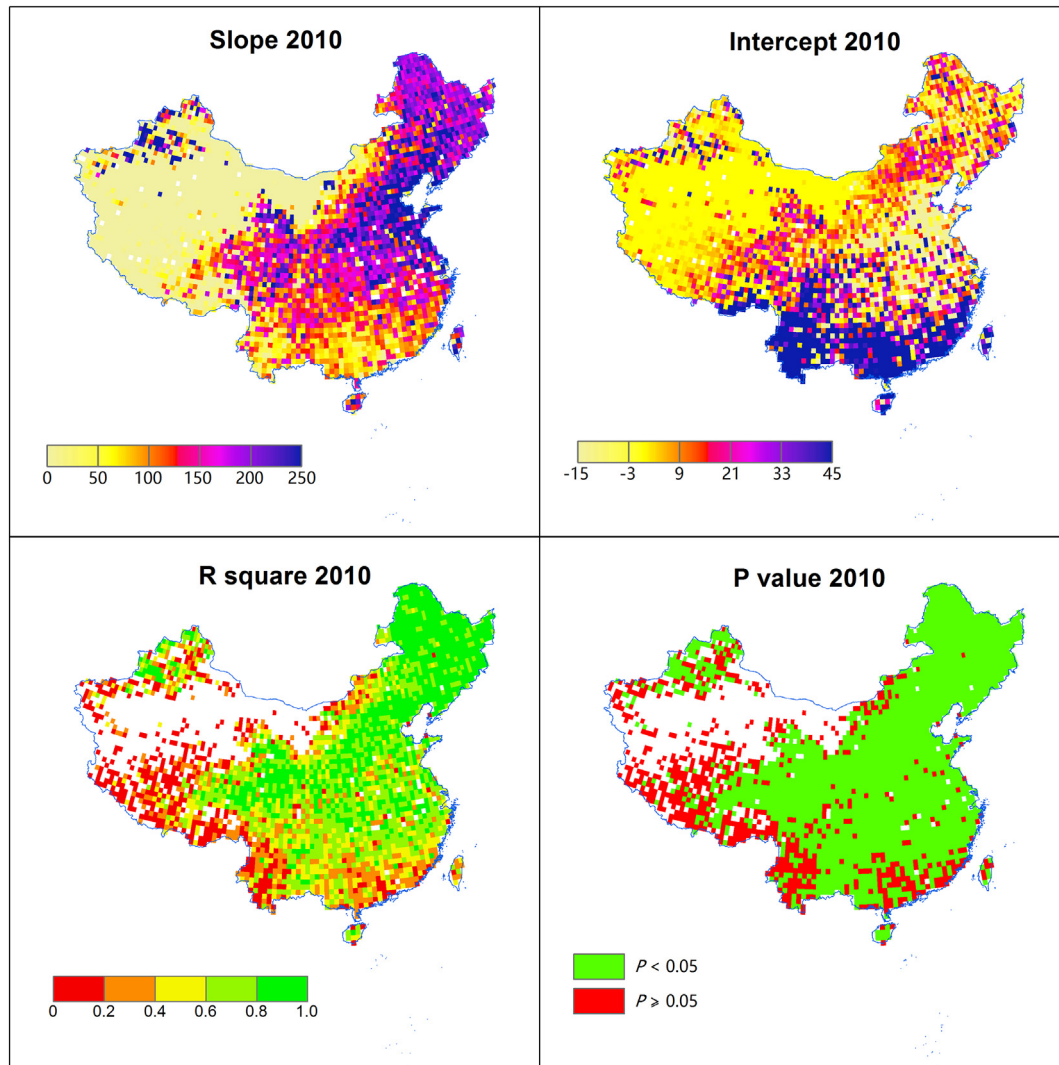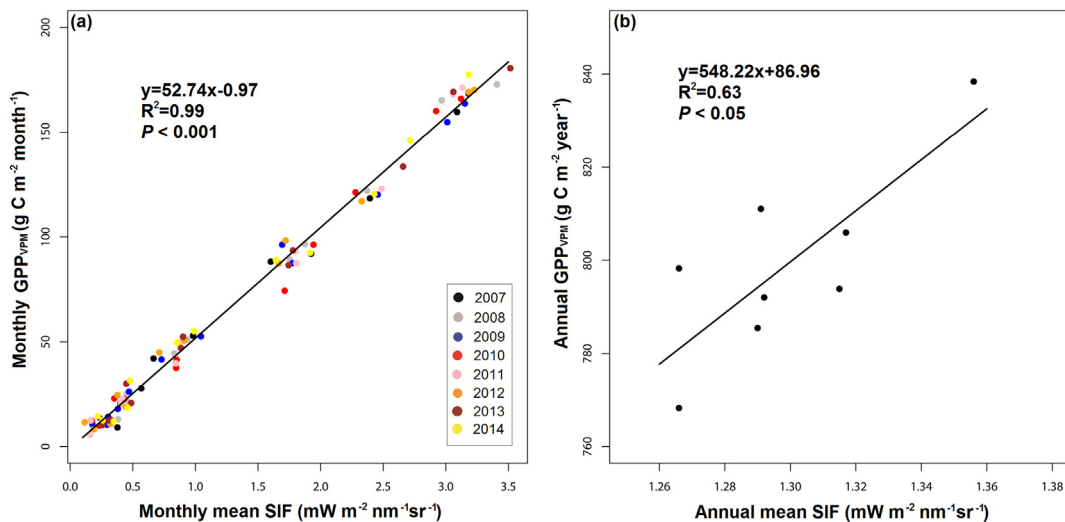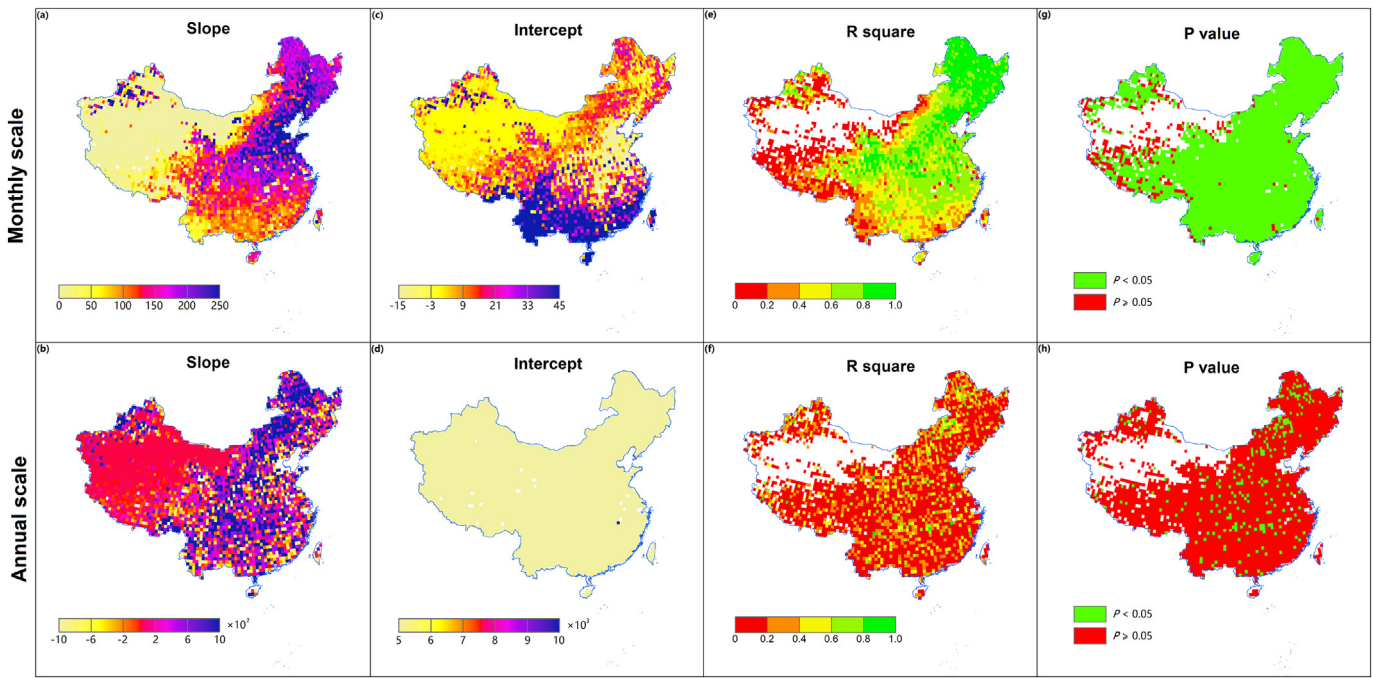
**Fig. 4.** The spatial distribution of statistical parameters of pixel-wise linear correlation between monthly GPP$_{VPM}$ and SIF in 2010. (a) Slope, (b) intercept, (c) R square, and (d) $p$ value.

photosynthesis usually occurs under the most suitable climate conditions, which cannot be reflected in NCEP climate data. The aggregated NCEP climate data (the spatial and temporal resolution of the used

data has been diminished from original data) may decrease the climate fluctuation with time and cover up the optimal condition for vegetation photosynthesis. Especially in some low latitude areas (such as South



**Fig. 5.** Relationship of VPM simulated GPP (GPP$_{VPM}$) and solar-induced chlorophyll fluorescence (SIF) in China during 2007–2014 at different time scales. (a) Monthly scale; and (b) yearly scale.
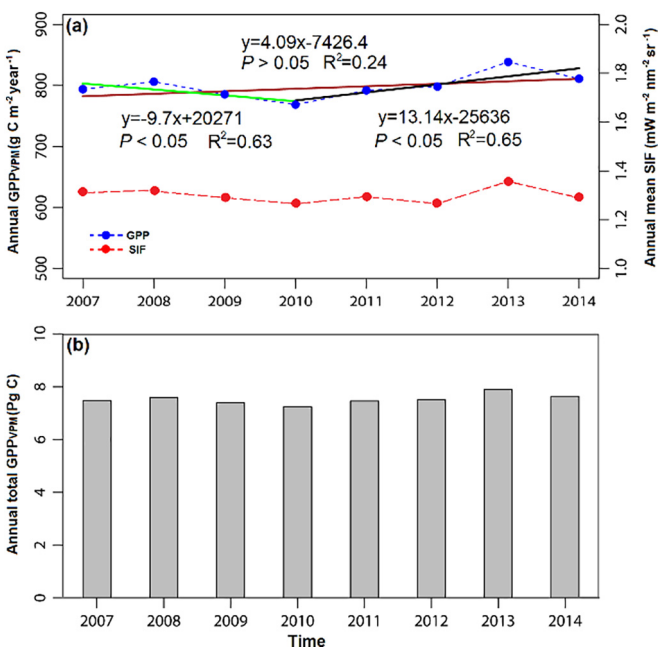
**Fig. 6.** Spatial distribution of statistical parameters of pixel-wise linear correlation between monthly GPP$_{VPM}$ and SIF and between annual GPP$_{VPM}$ and SIF during 2007–2014. (a) and (b) Slope, (c) and (d) Intercept, (e) and (f) R square, and (g) and (h) P value.

China), higher uncertainty of the emergence of the most suitable climate condition, derived by the low variance of climate, may lead to poor performance of maximum GPP simulation. For example, the VPM-simulated GPP, parameterized by the NCEP climate dataset, was compared with flux tower-based GPP at 39 flux site at 8-day interval in US, and the result showed that the maximum GPP$_{VPM}$ values of about 12 sites had been underestimated (Zhang et al., 2016c). Furthermore, Southern China has generally experienced frequent cloud cover,



**Fig. 7.** Interannual trends of VPM simulated GPP (GPP$_{VPM}$), solar-induced chlorophyll fluorescence (SIF), and annual total sequestrated C (calculated as the sum of GPP$_{VPM}$) in China during 2007–2014. (a) Annual dynamics of GPP$_{VPM}$ and SIF and the interannual trends of GPP$_{VPM}$ and SIF during 2007–2014, 2007–2010, and 2010–2014; and (b) Annual total sequestrated C for China during 2007–2014.

which may hinder the calculation of vegetation indices (such as EVI) using MODIS images (Nitze et al., 2015; Pinto et al., 2017).

GPP$_{VPM}$ is also consistent with SIF data at the seasonal timescale, and positive linear correlations exist for all seasons in 2010 (Fig. 3). However, the correlation in DJF is much weaker ($R^2 = 0.37$), which can be explained by lower SIF signal and relative lower signal-to-noise ratio in winter (Zhang et al., 2016c). Furthermore, a significant positive linear correlation exists between monthly GPP$_{VPM}$ and SIF in 2010 for most pixels in China (Fig. 4). This correlation also confirms that VPM simulated GPP matches the SIF data well in China for a single year. Note that small areas in Southwestern and Southern China have relatively low consistency between monthly GPP$_{VPM}$ and SIF in 2010 ($R^2 < 0.3$). This weak correlation could be attributed to the extreme droughts in Southwestern China during 2009–2012 (Zhou et al., 2017) and cloudy weather conditions Southern China which have been reported to cause significant decreases in vegetative productivity (Zhang et al., 2015; Zhao et al., 2015).

Moreover, relatively high consistency ($R^2 > 0.5$) exists between monthly GPP$_{VPM}$ and SIF during 2007–2014 for almost all pixels in China (Fig. 6), and monthly GPP$_{VPM}$ is also significantly positive linear correlated ($R^2 = 0.99$) with monthly SIF of the entire China (Fig. 5). These results indicate that GPP$_{VPM}$ not only matches SIF well for a single year, but is also strongly correlated with SIF at monthly scale for multiple years. Moreover, the $R^2$ value of monthly comparison ($R^2 = 0.99$) is generally higher than that of yearly comparison ($R^2 = 0.63$) for the entire China. Especially, most pixels of China did not have a significant ($P > 0.05$) correlation between GPP$_{VPM}$ and SIF data at annual time scale (Fig. 6f). This difference may be attributed to two reasons. First, large uncertainty exists in individual GOME-2 SIF grid cell which has extreme low spatial (0.5) and temporal (monthly) resolutions. Especially, when aggregating monthly data into yearly data, this uncertainty may be magnified. Second, the interannual variation is relatively small compare to the monthly variations due to sensor degradation occurred over the years, and GOME-2 SIF data are not recommended to be used in exploring inter-annual dynamics of vegetation photosynthesis (Joiner et al., 2014). High uncertainty in SIF and GPP estimates leads to lower correlation at inter-annual scale. Nevertheless, there remains a high consistency between GPP$_{VPM}$ and SIF at monthly and yearly scales for China.
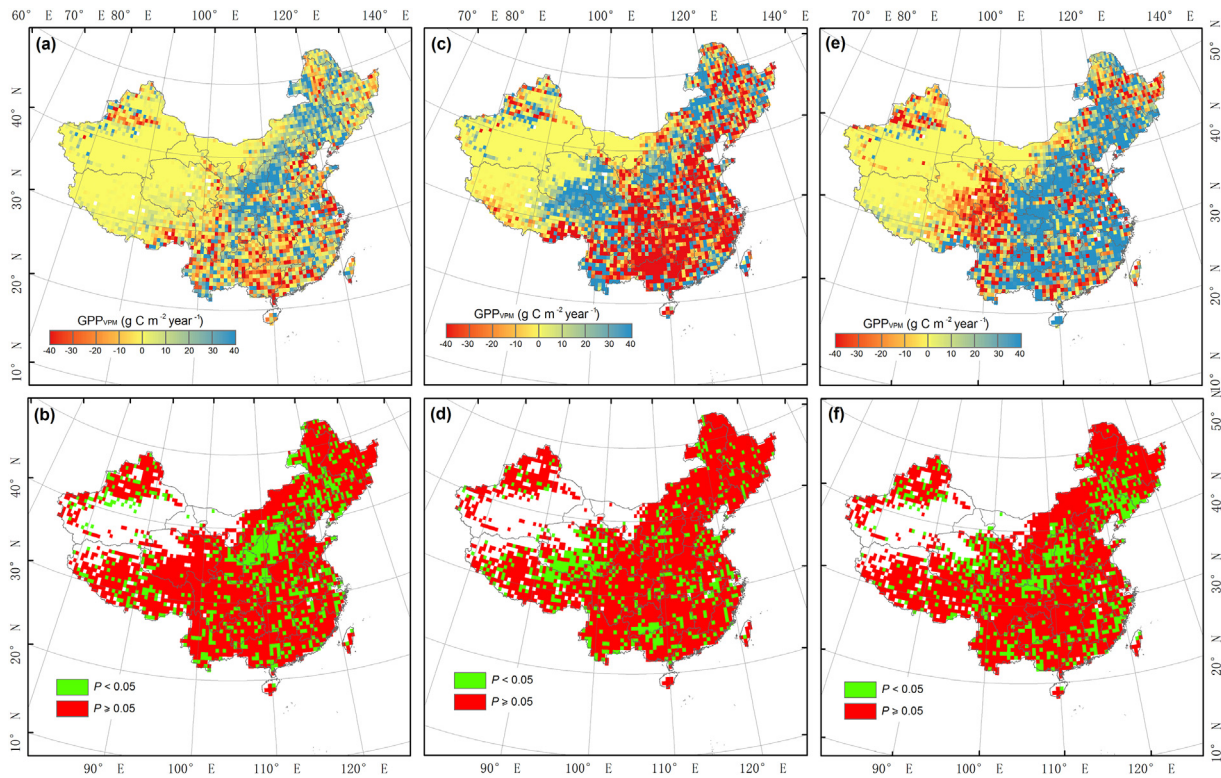
**Fig. 8.** The spatial distribution of slope values and *p* values of pixel-wise linear correlation between annual GPP$_{VPM}$ and time during 2007–2014, 2007–2010, and 2010–2014, respectively. (a) Slope value in 2007–2014, (b) p value in 2007–2014, (c) slope value in 2007–2010, (d) p value in 2007–2010, (e) slope value in 2010–2014, and (f) p value in 2010–2014.

In order to eliminate the effects of spatial mismatch (Y.G. Zhang et al. 2014) on the results of comparisons between GPP$_{VPM}$ and SIF data in our study, the GPP$_{VPM}$ dataset was aggregated into the same spatial resolution as GOME-2 SIF data (0.5°). From the pixel-wise linear correlation analysis between GPP$_{VPM}$ and SIF data, the correlation for most regions

of China was relative high ($R^2 > 0.5$). However, a high degree of spatial variability exists in the distribution of coefficient of determination, and the strongest correlation is largely distributed in Northeastern China and the North China Plains. The differences can be attributed to three aspects: (1) the spatial heterogeneity of land cover is low in
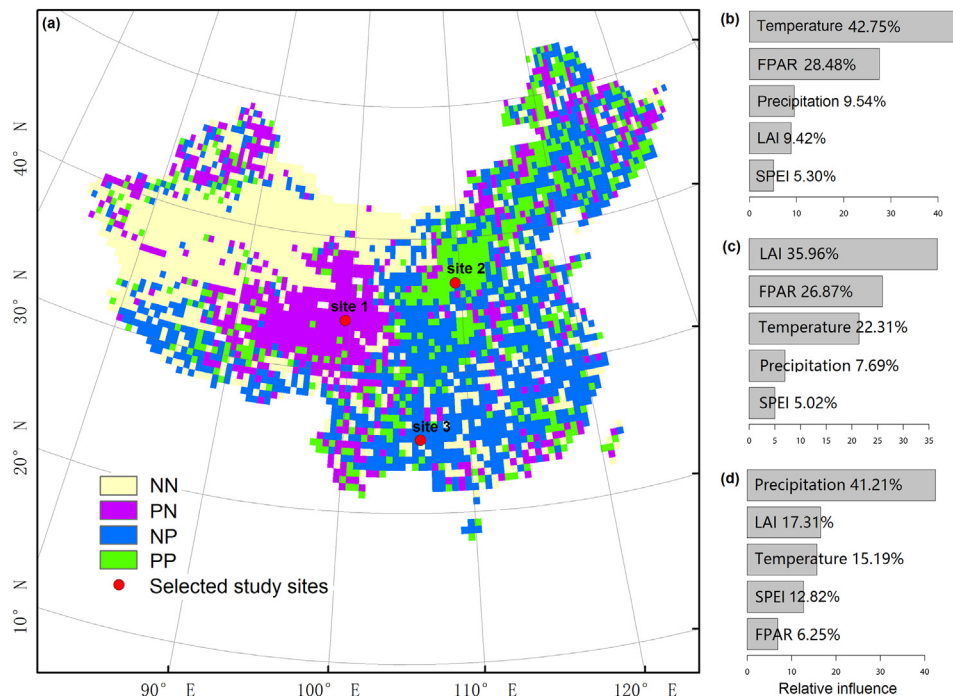


**Fig. 9.** The spatial distribution of different GPP$_{VPM}$ trend change types and the relative influence of climate and land cover variables on the GPP$_{VPM}$ trends of these types. The relative influence results were obtained using boosted regression tree (BRT) analysis. (a)Spatial distribution of different GPP$_{VPM}$ trend change types and selected typical study sites, (b) the relative influence of individual variables for site 1 with a PN type, (c) the relative influence of individual variables for site 2 with a PP type, and (d) the relative influence of individual variables for site 3 with a NP type. NN: continuously negative, PN: positive changed into negative, NP: negative changed into positive, and PP: continuously positive.

Northeastern and North China when compared to other regions (Kuang et al., 2016; Wu et al., 2008). For 0.5° spatial resolution, homogeneous pixels have less variance and uncertainty in presenting GPP than heterogeneous (mixed) pixels considering the VPM is parameterized biome-specifically; (2) the MODIS images in low latitude areas of China are contaminated more frequently by clouds and cloud shadows, which can decrease vegetation indices (Atkinson et al., 2012; Soudani et al., 2008) as well as solar irradiation (Eck and Dye, 1991); and (3) these regions are dominated by croplands which have a high photosynthesis seasonality. The relative signal to noise ratio in GOME-2 SIF data is higher for these regions.

Space-borne SIF data has been shown to have the potential to measure vegetative production by previous studies (Joiner et al., 2014; Wagle et al., 2016; Y.G. Zhang et al. 2014), which have compared satellite-derived SIF data with in-situ GPP estimates from eddy covariance flux tower sites. Emission of SIF occurs during photosynthesis, and SIF can be regarded as the direct observation of energy transmission during photochemical quenching (Flexas et al., 2000; Lee et al., 2015; Liu et al., 2016; Porcar-Castell et al., 2014). The VPM-simulated GPP generally presents high spatial-temporal consistency with GOME-2 SIF data during 2007–2014 in China. Therefore, space-borne SIF data has great potential in validating and parameterizing satellite-based GPP simulations at the regional scale.

### 4.2. Spatial-temporal dynamics of vegetation GPP in China

Apparent spatial heterogeneity is shown in the distribution of average annual GPP and maximum daily GPP in 2010 (Fig. 1). This spatial variability mostly corresponds to the difference in land cover distribution and the variance in the ability for ecosystems to uptake carbon. In this study, cropland and evergreen broadleaf forest are the dominant land cover type in the North China Plain and South China, and they are reported to have higher annual total GPP than other ecosystems (Beer et al., 2010; Frankenberg et al., 2011; Turner et al., 2006). Therefore, these attributes explain why the highest annual GPP value in 2010 can be found in these regions. However, the spatial pattern of maximum daily GPP in 2010 varies greatly from average annual GPP, and the highest value was distributed in Northeastern China and North China Plain where croplands (mainly maize) dominate. Maize is C4 crop, and it should definitely have the highest maximum daily GPP because C4 crops have higher LUE and water use efficiency (WUE) than other ecosystems (Lei and Yang, 2010; Zhang et al., 2007). Although South China shows the highest annual GPP, which mainly attributed to the long growing season, the maximum daily GPP is not very high. This variance is likely to be related with the simulation error in this region where correlation between GPP$_{VPM}$ and SIF is not as strong. South China is mainly dominated by evergreen vegetation, which shows extreme low variations of GPP and SIF. Considering the relatively large uncertainty in the SIF signal, the correlation between GPP and SIF would be low, which is also true for tropical rainforest (Zhang et al., 2016c).

Although GOME-2 SIF data is not appropriate for analyzing interannual variation due to the sensor degradation (Joiner et al., 2014), the dynamic trends of annual GPP$_{VPM}$ and annual mean SIF during 2007–2014 for China are similar (Fig. 7), both of which decline during 2007–2010 and increase during 2010–2014. This similarity indicates that VPM performs well in simulating annual GPP, which is also reflected by the significant positive linear correlation between annual GPP$_{VPM}$ and annual mean SIF during 2007–2014 for China (Fig.5). Spatially, vegetation production in China during 2007–2014 presents high heterogeneity (Fig. 8). GPP$_{VPM}$ in most areas of China displayed a decreasing trend during 2007–2010 and an increasing trend during 2010–2014, except for some regions in Eastern Qinghai-Tibet Plateau. Vegetation production in some regions of the Loess Plateau continuously increased during the entire study period 2007–2014. The causes of different dynamic trends of GPP$_{VPM}$ during different periods in 2007–2014 are complex and are likely to be attributed to the great spatial heterogeneity of climate, land cover changes, and major ecological projects across China.

Firstly, the large variance of GPP in Eastern Qinghai-Tibet Plateau during 2007–2010 and 2010–2014 is most likely due to vegetation phenology delay around 2006 (Zhang et al., 2013). Climate variables including temperature, FPAR, and precipitation totally have a relative influence of 78.77% on GPP$_{VPM}$ (Fig. 9). This indicates that climate condition has significant impact and controls vegetation productivity in this area. Precipitation accounts for a relative high influence (41.21%) of the GPP$_{VPM}$ dynamic in Southwestern China. This is in line with a study which reported that drought is considered as the most important factor in influencing China's GPP in recent years, especially in Southwestern China (Ju et al., 2010; Zhao et al., 2015). Moreover, land cover change (mainly urbanization) is regarded as another important factor that reduces GPP. The negative effects of urbanization on GPP are most obvious in the areas around metropolitan in China (such as Beijing and Shanghai, Fig. 8) (Cui et al., 2017). Lastly, the high influence of LAI (35.96%) on GPP$_{VPM}$ in the site where GPP$_{VPM}$ continuously increase during the whole period of 2007–2014 is most likely attributed to the conduction of some major ecological engineering projects in China, such as the Grain for Green Project (Liu et al., 2014) and the Three-North Shelter Forest Program (He et al., 2015). Rapid restoration of vegetation, reflected by LAI, might have contributed the most to the continuous increase of GPP in the Loess Plateau of China (Zhang et al., 2016a).

Compared with a previous study which described the spatial-temporal patterns of VPM-based GPP of North America in 2010 (Zhang et al., 2016c), the total area of high annual GPP (>2000 g C m$^{-2}$ year$^{-1}$) and maximum daily GPP (>20 g C m$^{-2}$ year$^{-1}$) in China is larger. However, China also has many large areas with extreme low values of annual GPP (about 33.1% pixels have values lower than 100 g C m$^{-2}$ year$^{-1}$) and maximum daily GPP (about 27.4% pixels have values lower than 5 g C m$^{-2}$ day$^{-1}$) (Fig. 1). Moreover, as estimated in this study, mean annual total sequestrated carbon (sum of GPP) of China ranged from approximately 7.52 Tg C km$^{-2}$ to 8.20 Tg C km$^{-2}$ (Fig. 7), which is larger than that of North America (6.76 Tg C km$^{-2}$). These results indicate that vegetation in China demonstrates a higher ability to sequester carbon, which can contribute to an in increasing global carbon sink. Protections should be adopted in some ecological vulnerable areas of China, especially in the Northwestern Desert and Tibet Plateau. Furthermore, annual total GPP shows a large increase when compared to the period during 1980–2000 (Fang et al., 2007). This trend demonstrates that terrestrial vegetation serves as an important carbon sink and plays a vital role in the global carbon cycle.

### 4.3. Implications of the application of GPP simulation using VPM

Based on the comparisons between GPP$_{VPM}$ and SIF at multiple spatial and temporal scales, the ability of VPM to simulate GPP in China varies among different regions. This variability demonstrates that the GPP$_{VPM}$ has been affected by some factors. Firstly, temperature and solar irradiation, can influence GPP estimates (Wagle et al., 2015). Temperature and solar irradiation directly determines the calculation of LUE and PAR, respectively, which will finally influence the GPP calculation. Secondly, land cover dataset (MODIS MCDQ12 land cover products) affect the estimation of biome-specific parameters of $\varepsilon_0$, $T_{min}$, $T_{max}$, and $T_{opt}$, which have impacts on the calculation of GPP. In this study, we use time-series MODIS land cover maps in the simulation of GPP during 2007–2014. However, MODIS land cover maps have some errors in identifying land cover changes over years (Friedl et al., 2010). Moreover, C3 and C4 crop types, which have different photosynthetic pathways, were not distinguished and will therefore have impacts on the estimation of LUE (Kalfas et al., 2011; Yuan et al., 2015). Each of these factors induce errors in the GPP simulation results. Thirdly, although a gap-fill algorithm has been applied in the calculation of GPP, MODIS image quality also influences the accuracy of GPP$_{VPM}$. Clouds and cloud

shadows at low latitude areas affects the quality of EVI, LSWI, and LST products, which are inputs in the VPM.

In this study, we assumed that the GOME-2 SIF data were direct observations of photosynthesis from space. However, the low spatial resolution (0.5°) of this SIF data has a certain impact on the comparison results. The comparisons between GPP$_{VPM}$ and SIF have to be conducted after GPP data are aggregated into the same spatial resolution as GOME-2 SIF data. The averaged GPP values of pixels ignore the extreme GPP values, and it will decrease the performance of comparisons between GPP$_{VPM}$ and SIF. However, space-borne SIF data still have great significance in estimating GPP simulations of LUE-based model. Simulation processes can be simplified and simulation accuracy can be enhanced when satellite-based SIF, with appropriate spatial resolution, are incorporated in the parameters.

## 5. Conclusion

In this study, GPP in China was simulated using VPM during 2007–2014, and comparisons between GPP$_{VPM}$ and GOME-2 SIF were also conducted. Monthly GPP$_{VPM}$ agrees with SIF data at both single-year and multi-year scales during 2007–2014. However, consistency between GPP$_{VPM}$ and SIF in the Northwest Desert, Tibet Plateau, and some areas in South China is relatively low. Moreover, GPP$_{VPM}$ is spatially correlated with SIF at the annual scale during 2007–2014, and correlations between GPP$_{VPM}$ and SIF were strong for all seasons except winter. In the period of 2007–2014, GPP$_{VPM}$ is likely to change from a negative trend into a positive trend around the year 2010, and climate and land cover conditions, including climate warming, drought, and vegetation restoration induced by major ecological projects in China, played important roles in affecting GPP$_{VPM}$ trends in different areas of China. In sum, space-borne SIF data is highly consistent with GPP$_{VPM}$ at both seasonal and annual scales, and SIF data has great potential in validating and parameterizing GPP estimates by LUE-based models.

Supplementary data to this article can be found online at https://doi.org/10.1016/j.scitotenv.2018.05.245.

## References

Atkinson, P.M., Jeganathan, C., Dash, J., Atzberger, C., 2012. Inter-comparison of four models for smoothing satellite sensor time-series data to estimate vegetation phenology. Remote Sens. Environ. 123, 400–417.

Baldocchi, D., Falge, E., Gu, L.H., Olson, R., Hollinger, D., Running, S., Anthoni, P., Bernhofer, C., Davis, K., Evans, R., Fuentes, J., Goldstein, A., Katul, G., Law, B., Lee, X.H., Malhi, Y., Meyers, T., Munger, W., Oechel, W., U, K.T.P., Pilegaard, K., Schmid, H.P., Valentini, R., Verma, S., Vesala, T., Wilson, K., Wofsy, S., 2001. FLUXNET: a new tool to study the temporal and spatial variability of ecosystem-scale carbon dioxide, water vapor, and energy flux densities. Bull. Am. Meteorol. Soc. 82, 2415–2434.

Ballantyne, A.P., Alden, C.B., Miller, J.B., Tans, P.P., White, J.W.C., 2012. Increase in observed net carbon dioxide uptake by land and oceans during the past 50 years. Nature 488 (70–+).

Beer, C., Reichstein, M., Tomelleri, E., Ciais, P., Jung, M., Carvalhais, N., Roedenbeck, C., Arain, M.A., Baldocchi, D., Bonan, G.B., Bondeau, A., Cescatti, A., Lasslop, G., Lindroth, A., Lomas, M., Luyssaert, S., Margolis, H., Oleson, K.W., Roupsard, O., Veenendaal, E., Viovy, N., Williams, C., Woodward, F.I., Papale, D., 2010. Terrestrial gross carbon dioxide uptake: global distribution and covariation with climate. Science 329, 834–838.

Chen, J.Q., Yan, H.M., Wang, S.Q., Gao, Y.N., Huang, M., Wang, J.B., Xiao, X.M., 2014. Estimation of gross primary productivity in Chinese terrestrial ecosystems by using VPM model. Quat. Sci. 34, 732–742.

Ciais, P., Reichstein, M., Viovy, N., Granier, A., Ogee, J., Allard, V., Aubinet, M., Buchmann, N., Bernhofer, C., Carrara, A., Chevallier, F., De Noblet, N., Friend, A.D., Friedlingstein, P., Grunwald, T., Heinesch, B., Keronen, P., Knohl, A., Krinner, G., Loustau, D., Manca, G., Matteucci, G., Miglietta, F., Ourcival, J.M., Papale, D., Pilegaard, K., Rambal, S., Seufert, G., Soussana, J.F., Sanz, M.J., Schulze, E.D., Vesala, T., Valentini, R., 2005. Europe-wide reduction in primary productivity caused by the heat and drought in 2003. Nature 437, 529–533.

Cui, Y., Xiao, X., Zhang, Y., Dong, J., Qin, Y., Doughty, R.B., Zhang, G., Wang, J., Wu, X., Qin, Y., Zhou, S., Joiner, J., Moore III, B., 2017. Temporal consistency between gross primary production and solarinduced chlorophyll fluorescence in the ten most populous megacity areas over years. Sci. Rep. 7, 14963.

Demmig-Adams, B., Adams, W.W., 2000. Photosynthesis - harvesting sunlight safely. Nature 403 (371–+).

Dong, J., Xiao, X., Wagle, P., Zhang, G., Zhou, Y., Jin, C., Torn, M.S., Meyers, T.P., Suyker, A.E., Wang, J., Yan, H., Biradar, C., Moore III, B., 2015. Comparison of four EVI-based models for estimating gross primary production of maize and soybean croplands and tallgrass prairie under severe drought. Remote Sens. Environ. 162, 154–168.

Eck, T.F., Dye, D.G., 1991. Satellite estimation of incident photosynthetically active radiation using ultraviolet reflectance. Remote Sens. Environ. 38, 135–146.

Elith, J., Leathwick, J.R., Hastie, T.A., 2008. Working guide to boosted regression trees. J. Anim. Ecol. 77, 802–813.

Fang, J.Y., Guo, Z.D., Piao, S.L., Chen, A.P., 2007. Terrestrial vegetation carbon sinks in China, 1981–2000. Sci. China Ser. D Earth Sci. 50, 1341–1350.

Flexas, J., Briantais, J.M., Cerovic, Z., Medrano, H., Moya, I., 2000. Steady-state and maximum chlorophyll fluorescence responses to water stress in grapevine leaves: a new remote sensing system. Remote Sens. Environ. 73, 283–297.

Frankenberg, C., Fisher, J.B., Worden, J., Badgley, G., Saatchi, S.S., Lee, J.-E., Toon, G.C., Butz, A., Jung, M., Kuze, A., Yokota, T., 2011. New global observations of the terrestrial carbon cycle from GOSAT: patterns of plant fluorescence with gross primary productivity. Geophys. Res. Lett. 38.

Frankenberg, C., O'Dell, C., Berry, J., Guanter, L., Joiner, J., Koehler, P., Pollock, R., Taylor, T.E., 2014. Prospects for chlorophyll fluorescence remote sensing from the orbiting carbon observatory-2. Remote Sens. Environ. 147, 1–12.

Friedl, M.A., Sulla-Menashe, D., Tan, B., Schneider, A., Ramankutty, N., Sibley, A., Huang, X., 2010. MODIS collection 5 global land cover: algorithm refinements and characterization of new datasets. Remote Sens. Environ. 114, 168–182.

Guan, K., Berry, J.A., Zhang, Y., Joiner, J., Guanter, L., Badgley, G., Lobell, D.B., 2016. Improving the monitoring of crop productivity using spaceborne solar-induced fluorescence. Glob. Chang. Biol. 22, 716–726.

Guanter, L., Frankenberg, C., Dudhia, A., Lewis, P.E., Gomez-Dans, J., Kuze, A., Suto, H., Grainger, R.G., 2012. Retrieval and global assessment of terrestrial chlorophyll fluorescence from GOSAT space measurements. Remote Sens. Environ. 121, 236–251.

Guanter, L., Zhang, Y., Jung, M., Joiner, J., Voigt, M., Berry, J.A., Frankenberg, C., Huete, A.R., Zarco-Tejada, P., Lee, J.-E., Moran, M.S., Ponce-Campos, G., Beer, C., Camps-Valls, G., Buchmann, N., Gianelle, D., Klumpp, K., Cescatti, A., Baker, J.M., Griffis, T.J., 2014. Global and time-resolved monitoring of crop photosynthesis with chlorophyll fluorescence. Proc. Natl. Acad. Sci. U. S. A. 111, E1327–E1333.

He, H., Liu, M., Xiao, X., Ren, X., Zhang, L., Sun, X., Yang, Y., Li, Y., Zhao, L., Shi, P., Du, M., Ma, Y., Ma, M., Zhang, Y., Yu, G., 2014. Large-scale estimation and uncertainty analysis of gross primary production in Tibetan alpine grasslands. J. Geophys. Res. Biogeosci. 119, 466–486.

He, B., Chen, A., Wang, H., Wang, Q., 2015. Dynamic response of satellite-derived vegetation growth to climate change in the three north shelter Forest region in China. Remote Sens. 7, 9998–10016.

Hilker, T., Coops, N.C., Wulder, M.A., Black, T.A., Guy, R.D., 2008. The use of remote sensing in light use efficiency based models of gross primary production: a review of current status and future requirements. Sci. Total Environ. 404, 411–423.

Huete, A., Didan, K., Miura, T., Rodriguez, E.P., Gao, X., Ferreira, L.G., 2002. Overview of the radiometric and biophysical performance of the MODIS vegetation indices. Remote Sens. Environ. 83, 195–213.

Jin, C., Xiao, X., Merbold, L., Arneth, A., Veenendaal, E., Kutsch, W.L., 2013. Phenology and gross primary production of two dominant savanna woodland ecosystems in southern Africa. Remote Sens. Environ. 135, 189–201.

Jin, C., Xiao, X., Wagle, P., Griffis, T., Dong, J., Wu, C., Qin, Y., Cook, D.R., 2015. Effects of in-situ and reanalysis climate data on estimation of cropland gross primary production using the vegetation photosynthesis model. Agric. For. Meteorol. 213, 240–250.

Joiner, J., Yoshida, Y., Vasilkov, A.P., Yoshida, Y., Corp, L.A., Middleton, E.M., 2011. First observations of global and seasonal terrestrial chlorophyll fluorescence from space. Biogeosciences 8, 637–651.

Joiner, J., Guanter, L., Lindstrot, R., Voigt, M., Vasilkov, A.P., Middleton, E.M., Huemmrich, K.F., Yoshida, Y., Frankenberg, C., 2013. Global monitoring of terrestrial chlorophyll fluorescence from moderate-spectral-resolution near-infrared satellite measurements: methodology, simulations, and application to GOME-2. Atmos. Meas. Tech. 6, 2803–2823.

Joiner, J., Yoshida, Y., Vasilkov, A., Schaefer, K., Jung, M., Guanter, L., Zhang, Y., Garrity, S., Middleton, E.M., Huemmrich, K.F., Gu, L., Marchesini, L.B., 2014. The seasonal cycle of satellite chlorophyll fluorescence observations and its relationship to vegetation phenology and ecosystem atmosphere carbon exchange. Remote Sens. Environ. 152, 375–391.

Ju, W., Wang, S., Yu, G., Zhou, Y., Wang, H., 2010. Modeling the impact of drought on canopy carbon and water fluxes for a subtropical evergreen coniferous plantation in southern China through parameter optimization using an ensemble Kalman filter. Biogeosciences 7, 845–857.

Jung, M., Vetter, M., Herold, M., Churkina, G., Reichstein, M., Zaehle, S., Ciais, P., Viovy, N., Bondeau, A., Chen, Y., Trusilova, K., Feser, F., Heimann, M., 2007. Uncertainties of modeling gross primary productivity over Europe: a systematic study on the effects of using different drivers and terrestrial biosphere models. Glob. Biogeochem. Cycles 21.

Jung, M., Reichstein, M., Bondeau, A., 2009. Towards global empirical upscaling of FLUXNET eddy covariance observations: validation of a model tree ensemble approach using a biosphere model. Biogeosciences 6, 2001–2013.

Jung, M., Reichstein, M., Margolis, H.A., Cescatti, A., Richardson, A.D., Arain, M.A., Arneth, A., Bernhofer, C., Bonal, D., Chen, J., Gianelle, D., Gobron, N., Kiely, G., Kutsch, W.,

Lasslop, G., Law, B.E., Lindroth, A., Merbold, L., Montagnani, L., Moors, E.J., Papale, D., Sottocornola, M., Vaccari, F., Williams, C., 2011. Global patterns of land-atmosphere fluxes of carbon dioxide, latent heat, and sensible heat derived from eddy covariance, satellite, and meteorological observations. J. Geophys. Res. Biogeosci. 116.

Kalfas, J.L., Xiao, X., Vanegas, D.X., Verma, S.B., Suyker, A.E., 2011. Modeling gross primary production of irrigated and rain-fed maize using MODIS imagery and $CO_2$ flux tower data. Agric. For. Meteorol. 151, 1514–1528.

Kuang, W., Liu, J., Dong, J., Chi, W., Zhang, C., 2016. The rapid and massive urban and industrial land expansions in China between 1990 and 2010: a CLUD-based analysis of their trajectories, patterns, and drivers. Landsc. Urban Plan. 145, 21–33.

Lee, J.-E., Berry, J.A., Van der Tol, C.S., Yang, X., Guanter, L., Damm, A., Baker, I., Frankenberg, C., 2015. Simulations of chlorophyll fluorescence incorporated into the community land model version 4. Glob. Chang. Biol. 21, 3469–3477.

Lei, H.-M., Yang, D.-W., 2010. Seasonal and interannual variations in carbon dioxide exchange over a cropland in the North China plain. Glob. Chang. Biol. 16, 2944–2957.

Li, Z., Liu, S., Tan, Z., Bliss, N.B., Young, C.J., West, T.O., Ogle, S.M., 2014. Comparing cropland net primary production estimates from inventory, a satellite-based model, and a process-based model in the midwest of the United States. Ecol. Model. 277, 1–12.

Liu, J., Cheng, Z., 2010. Detection of vegetation light-use efficiency based on solar-induced chlorophyll fluorescence separated from canopy radiance spectrum. IEEE J. Sel. Top. Appl. Earth Obs. Remote Sens. 3, 306–312.

Liu, J., Kuang, W., Zhang, Z., Xu, X., Qin, Y., Ning, J., Zhou, W., Zhang, S., Li, R., Yan, C., Wu, S., Shi, X., Jiang, N., Yu, D., Pan, X., Chi, W., 2014. Spatiotemporal characteristics, patterns, and causes of land-use changes in China since the late 1980s. J. Geogr. Sci. 24, 195–210.

Liu, L., Liu, X., Wang, Z., Zhang, B., 2016. Measurement and analysis of bidirectional SIF emissions in wheat canopies. IEEE Trans. Geosci. Remote Sens. 54, 2640–2651.

Ma, J., Xiao, X., Qin, Y., Chen, B., Hu, Y., Li, X., Zhao, B., 2017. Estimating aboveground biomass of broadleaf, needleleaf, and mixed forests in northeastern China through analysis of 25-m ALOS/PALSAR mosaic data. For. Ecol. Manag. 2017 (389), 199–210.

Monteith, J.L., 1972. Solar-radiation and productivity in tropical ecosystems. J. Appl. Ecol. 9, 747–766.

Nightingale, J.M., Coops, N.C., Waring, R.H., Hargrove, W.W., 2007. Comparison of MODIS gross primary production estimates for forests across the USA with those generated by a simple process model, 3-PGS. Remote Sens. Environ. 109, 500–509.

Nitze, I., Barrett, B., Cawkwell, F., 2015. Temporal optimisation of image acquisition for land cover classification with random Forest and MODIS time-series. Int. J. Appl. Earth Obs. Geoinf. 34, 136–146.

Pinto, D.G., Fontana, D.C., Dalmago, G.A., da Cunha, G.R., Fochesato, E., Vicari, M.B., de Gouvea, J.A., Santi, A., 2017. Temporal dynamics of spectral reflectance and vegetation indices during canola crop cycle in southern Brazil. Cienc. Rural 47.

Porcar-Castell, A., Tyystjarvi, E., Atherton, J., van der Tol, C., Flexas, J., Pfuendel, E.E., Moreno, J., Frankenberg, C., Berry, J.A., 2014. Linking chlorophyll a fluorescence to photosynthesis for remote sensing applications: mechanisms and challenges. J. Exp. Bot. 65, 4065–4095.

Potter, C.S., Randerson, J.T., Field, C.B., Matson, P.A., Vitousek, P.M., Mooney, H.A., Klooster, S.A., 1993. Terrestrial ecosystem production - a process model-based on global satellite and surface data. Glob. Biogeochem. Cycles 7, 811–841.

R Development Core Team, 2013. R: A Language and Environment for Statistical Computing. R Foundation for Statistical Computing (p. Vienna).

Raich, J.W., Rastetter, E.B., Melillo, J.M., Kicklighter, D.W., Steudler, P.A., Peterson, B.J., Grace, A.L., Moore, B., Vorosmarty, C.J., 1991. Potential net primary productivity in south-america - application of a global-model. Ecol. Appl. 1, 399–429.

Rogers, A., Medlyn, B.E., Dukes, J.S., Bonan, G., von Caemmerer, S., Dietze, M.C., Kattge, J., Leakey, A.D.B., Mercado, L.M., Niinemets, U., Prentice, I.C., Serbin, S.P., Sitch, S., Way, D.A., Zaehle, S., 2017. A roadmap for improving the representation of photosynthesis in earth system models. New Phytol. 213, 22–42.

Running, S.W., Nemani, R.R., Heinsch, F.A., Zhao, M.S., Reeves, M., Hashimoto, H., 2004. A continuous satellite-derived measure of global terrestrial primary production. Bioscience 54, 547–560.

Sitch, S., Smith, B., Prentice, I.C., Arneth, A., Bondeau, A., Cramer, W., Kaplan, J.O., Levis, S., Lucht, W., Sykes, M.T., Thonicke, K., Venevsky, S., 2003. Evaluation of ecosystem dynamics, plant geography and terrestrial carbon cycling in the LPJ dynamic global vegetation model. Glob. Chang. Biol. 9, 161–185.

Soudani, K., le Maire, G., Dufrene, E., Francois, C., Delpierre, N., Ulrich, E., Cecchini, S., 2008. Evaluation of the onset of green-up in temperate deciduous broadleaf forests derived from moderate resolution imaging spectroradiometer (MODIS) data. Remote Sens. Environ. 112, 2643–2655.

Turner, D.P., Ritts, W.D., Cohen, W.B., Gower, S.T., Running, S.W., Zhao, M.S., Costa, M.H., Kirschbaum, A.A., Ham, J.M., Saleska, S.R., Ahl, D.E., 2006. Evaluation of MODIS NPP and GPP products across multiple biomes. Remote Sens. Environ. 102, 282–292.

Vicente-Serrano, S.M., Beguería, Santiago, López-Moreno, Juan I., 2010. A multi-scalar drought index sensitive to global warming: the standardized precipitation evapotranspiration index - SPEI. J. Clim. 23, 1696–1718.

Wagle, P., Xiao, X., Torn, M.S., Cook, D.R., Matamala, R., Fischer, M.L., Jin, C., Dong, J., Biradar, C., 2014. Sensitivity of vegetation indices and gross primary production of tallgrass prairie to severe drought. Remote Sens. Environ. 152, 1–14.

Wagle, P., Xiao, X., Suyker, A.E., 2015. Estimation and analysis of gross primary production of soybean under various management practices and drought conditions. ISPRS J. Photogramm. Remote Sens. 99, 70–83.

Wagle, P., Zhang, Y., Jin, C., Xiao, X., 2016. Comparison of solar-induced chlorophyll fluorescence, light-use efficiency, and process-based GPP models in maize. Ecol. Appl. 26, 1211–1222.

Wu, W., Shibasaki, R., Yang, P., Ongaro, L., Zhou, Q., Tang, H., 2008. Validation and comparison of 1 km global land cover products in China. Int. J. Remote Sens. 29, 3769–3785.

Wu, C., Munger, J.W., Niu, Z., Kuang, D., 2010. Comparison of multiple models for estimating gross primary production using MODIS and eddy covariance data in Harvard Forest. Remote Sens. Environ. 114, 2925–2939.

Wu, C., Chen, J.M., Huang, N., 2011. Predicting gross primary production from the enhanced vegetation index and photosynthetically active radiation: evaluation and calibration. Remote Sens. Environ. 115, 3424–3435.

Xiao, X.M., Boles, S., Liu, J.Y., Zhuang, D.F., Liu, M.L., 2002. Characterization of forest types in northeastern China, using multi-temporal SPOT-4 VEGETATION sensor data. Remote Sens. Environ. 82, 335–348.

Xiao, X.M., Hollinger, D., Aber, J., Goltz, M., Davidson, E.A., Zhang, Q.Y., Moore, B., 2004a. Satellite-based modeling of gross primary production in an evergreen needleleaf forest. Remote Sens. Environ. 89, 519–534.

Xiao, X.M., Zhang, Q.Y., Braswell, B., Urbanski, S., Boles, S., Wofsy, S., Berrien, M., Ojima, D., 2004b. Modeling gross primary production of temperate deciduous broadleaf forest using satellite images and climate data. Remote Sens. Environ. 91, 256–270.

Xiao, X.M., Zhang, Q.Y., Saleska, S., Hutyra, L., De Camargo, P., Wofsy, S., Frolking, S., Boles, S., Keller, M., Moore, B., 2005. Satellite-based modeling of gross primary production in a seasonally moist tropical evergreen forest. Remote Sens. Environ. 94, 105–122.

Xiao, J., Zhuang, Q., Law, B.E., Chen, J., Baldocchi, D.D., Cook, D.R., Oren, R., Richardson, A.D., Wharton, S., Ma, S., Martin, T.A., Verma, S.B., Suyker, A.E., Scott, R.L., Monson, R.K., Litvak, M., Hollinger, D.Y., Sun, G., Davis, K.J., Bolstad, P.V., Burns, S.P., Curtis, P.S., Drake, B.G., Falk, M., Fischer, M.L., Foster, D.R., Gu, L., Hadley, J.L., Katul, G.G., Matamala, R., Mcnulty, S., Meyers, T.P., Munger, J.W., Noormets, A., Oechel, W.C., Paw, U.K.T., Schmid, H.P., Starr, G., Torn, M.S., Wofsy, S.C., 2010. A continuous measure of gross primary production for the conterminous United States derived from MODIS and AmeriFlux data. Remote Sens. Environ. 114, 576–591.

Xiao, J., Ollinger, S.V., Frolking, S., Hurtt, G.C., Hollinger, D.Y., Davis, K.J., Pan, Y., Zhang, X., Deng, F., Chen, J., Baldocchi, D.D., Law, B.E., Arain, M.A., Desai, A.R., Richardson, A.D., Sun, G., Amiro, B., Margolis, H., Gu, L., Scott, R.L., Blanken, P.D., Suyker, A.E., 2014. Data-driven diagnostics of terrestrial carbon dynamics over North America. Agric. For. Meteorol. 197, 142–157.

Yan, H., Fu, Y., Xiao, X., Huang, H.Q., He, H., Ediger, L., 2009. Modeling gross primary productivity for winter wheat-maize double cropping system using MODIS time series and $CO_2$ eddy flux tower data. Agric. Ecosyst. Environ. 129, 391–400.

Yang, X., Tang, J., Mustard, J.F., Lee, J.-E., Rossini, M., Joiner, J., Munger, J.W., Kornfeld, A., Richardson, A.D., 2015. Solar-induced chlorophyll fluorescence that correlates with canopy photosynthesis on diurnal and seasonal scales in a temperate deciduous forest. Geophys. Res. Lett. 42, 2977–2987.

Yuan, W., Liu, S., Zhou, G., Zhou, G., Tieszen, L.L., Baldocchi, D., Bernhofer, C., Gholz, H., Goldstein, A.H., Goulden, M.L., Hollinger, D.Y., Hu, Y., Law, B.E., Stoy, P.C., Vesala, T., Wofsy, S.C., Ameriflux, C., 2007. Deriving a light use efficiency model from eddy covariance flux data for predicting daily gross primary production across biomes. Agric. For. Meteorol. 143, 189–207.

Yuan, W., Cai, W., Nguy-Robertson, A.L., Fang, H., Suyker, A.E., Chen, Y., Dong, W., Liu, S., Zhang, H., 2015. Uncertainty in simulating gross primary production of cropland ecosystem from satellite-based models. Agric. For. Meteorol. 207, 48–57.

Yuan, W., Chen, Y., Xia, J., Dong, W., Magliulo, V., Moors, E., Olesen, J.E., Zhang, H., 2016. Estimating crop yield using a satellite-based light use efficiency model. Ecol. Indic. 60, 702–709.

Zhang, W.L., Chen, S.P., Chen, J., Wei, L., Han, X.G., Lin, G.H., 2007. Biophysical regulations of carbon fluxes of a steppe and a cultivated cropland in semiarid Inner Mongolia. Agric. For. Meteorol. 146, 216–229.

Zhang, G., Zhang, Y., Dong, J., Xiao, X., 2013. Green-up dates in the Tibetan plateau have continuously advanced from 1982 to 2011. Proc. Natl. Acad. Sci. U. S. A. 110, 4309–4314.

Zhang, Y.G., Guanter, L., Berry, J.A., Joiner, J., van der Tol, C., Huete, A., Gitelson, A., Voigt, M., Koehler, P., 2014a. Estimation of vegetation photosynthetic capacity from space-based measurements of chlorophyll fluorescence for terrestrial biosphere models. Glob. Chang. Biol. 20, 3727–3742.

Zhang, Y.L., Song, C.H., Zhang, K.R., Cheng, X.L., Zhang, Q.F., 2014b. Spatial-temporal variability of terrestrial vegetation productivity in the Yangtze River basin during 2000–2009. J. Plant Ecol. 7, 10–23.

Zhang, Y., Li, W., Zhu, Q., Chen, H., Fang, X., Zhang, T., Zhao, P., Peng, C., 2015. Monitoring the impact of aerosol contamination on the drought-induced decline of gross primary productivity. Int. J. Appl. Earth Obs. Geoinf. 36, 30–40.

Zhang, Y., Peng, C., Li, W., Tian, L., Zhu, Q., Chen, H., Fang, X., Zhang, G., Liu, G., Mu, X., Li, Z., Li, S., Yang, Y., Wang, J., Xiao, X., 2016a. Multiple afforestation programs accelerate the greenness in the 'Three North' region of China from 1982 to 2013. Ecol. Indic. 61, 404–412.

Zhang, Y., Xiao, X., Guanter, L., Zhou, S., Ciais, P., Joiner, J., Sitch, S., Wu, X., Nabel, J., Dong, J., Kato, E., Jain, A.K., Wiltshire, A., Stocker, B.D., 2016b. Precipitation and carbon-water coupling jointly control the interannual variability of global land gross primary production. Sci. Rep. 6.

Zhang, Y., Xiao, X., Jin, C., Dong, J., Zhou, S., Wagle, P., Joiner, J., Guanter, L., Zhang, Y., Zhang, G., Qin, Y., Wang, J., Moore III, B., 2016c. Consistency between sun-induced chlorophyll fluorescence and gross primary production of vegetation in North America. Remote Sens. Environ. 183, 154–169.

Zhang, G.L., Xiao, X.M., Biradar, C.M., Dong, J.W., Qin, Y.W., Menarguez, M.A., Zhou, Y.T., Zhang, Y., Jin, C., Wang, J., Doughty, R.B., Ding, M.J., Moore, B., 2017. Spatiotemporal patterns of paddy rice croplands in China and India from 2000 to 2015. Sci. Total Environ. 579, 82–92.

Zhao, M.S., Heinsch, F.A., Nemani, R.R., Running, S.W., 2005. Improvements of the MODIS terrestrial gross and net primary production global data set. Remote Sens. Environ. 95, 164–176.

Zhao, M., Running, S.W., Nemani, R.R., 2006. Sensitivity of Moderate Resolution Imaging Spectroradiometer (MODIS) terrestrial primary production to the accuracy of meteorological reanalyses. J. Geophys. Res. Biogeosci. 111.

Zhao, Z., Wu, X., Li, G., Li, J., 2015. Drought in southwestern China and its impact on the net primary productivity of vegetation from 2009–2011. Acta Ecol. Sin. 35, 350–360.

Zhou, L., Wu, J., Mo, X., Zhou, H., Diao, C., Wang, Q., Chen, Y., Zhang, F., 2017. Quantitative and detailed spatiotemporal patterns of drought in China during 2001–2013. Sci. Total Environ. 589, 136–145.

Zhu, Z., Bi, J., Pan, Y., Ganguly, S., Anav, A., Xu, L., Samata, A., Piao, S.L., Nemani, R.R., Myneni, R.B., 2013. Global data sets of vegetation leaf area index (LAI)3g and fraction of photosynthetically active radiation (FPAR)3g derived from global inventory modeling and mapping studies (GIMMS) normalized difference vegetation index (NDVI3g) for the period 1981 to 2011. Remote Sens. 5, 927–948.